



Cite this: *Nanoscale*, 2019, **11**, 2703

High-efficiency modulation of coupling between different polaritons in an in-plane graphene/hexagonal boron nitride heterostructure†

Xiangdong Guo,^{a,b,c,d} Hai Hu,^{a,c} Debo Hu,^a Baoxin Liao,^{a,c} Ke Chen,^{a,c} Lei Liu,^e Xing Zhu,^{a,b,d} Xiaoxia Yang^{*a,c} and Qing Dai^{ib *a,c}

Two-dimensional van der Waals (vdW) materials have a full set of highly confined polariton modes, such as low-loss phonon polaritons and dynamically tunable graphene plasmons, which provide a solution for integrated nanophotonic devices by combining the unique advantages of different polaritons. Highly efficient coupling between these complementary polaritons is key to realize the nanoscale optical integration. However, fluctuations of permittivity or geometry at the abrupt interfaces have been demonstrated as perturbations or scatters of polaritons. Here, in-plane plasmon–phonon polariton coupling in an in-plane graphene/hexagonal boron nitride (BN) heterostructure is studied using a full-wave electromagnetic numerical model. Transmittance between different polaritons is proportional to momentum matching, which can be tuned using the graphene Fermi energy. The transmittance between a graphene plasmon and a BN phonon polariton can be controlled between 0% and 100% within the upper Reststrahlen band of the BN. This is central to many photon devices, such as waveguides, wavefront shapers, filters, modulators and switches. Moreover, we simulate near-field interference patterns in an in-plane heterostructure based on the theoretical dispersion relation of polaritons, enabling scattering scanning near-field optical microscopy a potential experimental method to investigate the coupling between different polaritons. This study provides a theoretical basis for efficient coupling of propagation and modulation between different polaritons in in-plane heterostructures of vdW materials, which could pave a way to design nanoscale multi-functional waveguide devices in integrated photonic systems.

Received 15th October 2018,

Accepted 6th January 2019

DOI: 10.1039/c8nr08334g

rsc.li/nanoscale

Introduction

Emerging telecommunication and data routing applications require ultra-compact photonic integrated circuits.^{1,2} Polaritons supported at interfaces between media with permittivities of opposite signs can break the diffraction limit, allowing light to be confined and manipulated at the nanoscale.^{3–6} Polaritons in two-dimensional (2D) van der Waals (vdW)

materials have been widely studied recently,^{7–9} such as plasmon polaritons in graphene^{10,11} and black phosphorus,^{12,13} exciton polaritons in MoSe₂,¹⁴ and phonon polaritons in hexagonal boron nitride (BN).^{15,16} These polaritons in vdW systems have demonstrated the highest degree of confinement among all the known materials as well as many other complementary virtues, such as electrical tunability of the graphene plasmon (GP),^{17–20} anisotropy plasmonic performance of black phosphorus,^{21,22} and a low loss long-distance propagation performance of BN phonon polaritons.^{23–25} These advantages enable a platform for strong light–matter interactions and efficient polaritonic waveguides, which have great potential in enhanced infrared sensing,^{26–31} sub-diffractive optical focusing and imaging,^{32,33} and hyperbolic optical metasurfaces.⁵ Moreover, vdW heterostructures can be designed by assembling different vdW layers at the level of single atomic planes, enabling unparalleled control of each polariton and new electromagnetic modes by coupling of different brands of polaritons.^{7–9} For example, GPs can interact with phonon polaritons or phonons in underlying polar substrates such as BN^{24,34,35} or SiO₂,^{36,37} and the resulting hybri-

^aDivision of Nanophotonics, CAS Center for Excellence in Nanoscience, National Center for Nanoscience and Technology, Beijing 100190, P. R. China.

E-mail: daiq@nanocr.cn, yangxx@nanocr.cn; Tel: +86-010-82545720

^bAcademy for Advanced Interdisciplinary Studies, Peking University, Beijing 100871, P. R. China

^cCenter of Materials Science and Optoelectronics Engineering, University of Chinese Academy of Sciences, Beijing 100049, P. R. China

^dState Key Lab for Mesoscopic Physics, School of Physics, Peking University, Beijing 100871, P. R. China

^eCollege of Engineering, Peking University, Beijing 100871, P. R. China

†Electronic supplementary information (ESI) available. See DOI: 10.1039/c8nr08334g

dized polaritons inherit electrostatic tunability from the graphene and long lifetimes from the phonons.³⁴

Besides the out-of-plane coupling of different polaritons by vertically stacking vdW materials together, integrating them in the plane is also a promising route toward more compact and efficient integrated photonic circuits.^{38,39} In previous studies, improved polariton excitation, modulation, and functions have been found in lateral structures.^{39,40} For example, by integrating tapered SiC with graphene, the excitation efficiency of GPs can be effectively improved to 25% *via* compressing surface polaritons in tapered SiC.³⁹ Coupling BN phonon polaritons over a graphene-covered gap can give a modulation depth of 14–20 dB by gating the graphene.⁴⁰ A lateral device was proposed to use edge-free carbon nanotubes as a low-loss plasmon waveguide and the graphene disk as a tunable coupling modulator.³⁸ All the functions described above also depend on the out-of-plane coupling of polaritons in the overlapping region, but geometrical discontinuity decreases the coupling efficiency because of electromagnetic scattering at the interface.^{38,39} To avoid this side effect and develop atomic-thin-layer integrated circuits, many efforts have been invested to fabricate an in-plane heterostructure by epitaxial growth, in which two different vdW materials are seamlessly stitched together.^{41–44} For example, monolayer BN was heteroepitaxially grown on graphene edges through the chemical vapor deposition method due to their close crystal lattice match (1.7%).⁴¹ However, there is a lack of study on polariton propagating behaviors in an in-plane seamlessly connected heterostructure and the transmittance at the interfaces of different vdW materials is not clear.

Here, we study the transmission of graphene plasmons and BN phonon polaritons at the interface of the graphene/BN in-plane heterostructure by the finite element method (FEM) and propose a full-wave electromagnetic numerical model of in-plane plasmon–phonon polariton coupling. The numerical model avoids the complex electromagnetic field boundary conditions at the heterostructure interface required in the analytical theory and can solve the coupling between different polaritons by accurate waveguide mode analysis.⁴⁵ We find that transmittance is mainly determined by the difference in the momentums of different polaritons, which increases as the momentum difference decreases. Tuning the momentum matching conditions by changing the graphene Fermi energy allows a wide range of transmittance modulations, from 0% to 100%, to be achieved. To quantitatively characterize the electromagnetic field distribution at the interface during the transmission process, the near-field interference patterns of polaritons are simulated based on their theoretical dispersion relation. Transmittance analysis of the near-field interference patterns is consistent with the results of the previous numerical model, meaning that scattering scanning near-field optical microscopy (s-SNOM) could be used to study polariton coupling. This study provides a theoretical basis for developing ultracompact polariton circuitry and multi-functional polariton devices based on 2D vdW heterostructures.

Results and discussion

The graphene/BN in-plane heterostructure is schematically displayed in Fig. 1a. The close match (1.7% different) between the graphene and BN lattices means that the materials can be integrated with coherent lattices.⁴¹ For simplicity, the freestanding graphene/BN in-plane heterostructure is considered and the graphene has uniform charge density. The graphene and BN can support the plasmon and hyperbolic phonon polariton (HPP), respectively. When the propagating plasmon (phonon) polariton reaches the graphene–BN interface, they can reflect back or transmit into phonon (plasmon) polaritons in the other side.

The electromagnetic responses of graphene and BN can be exhibited by the frequency (ω)/momentum (q) dispersion relations of their polariton modes. The dispersion curves can be represented as the imaginary part of the Fresnel reflection coefficient $r_p(q, \omega)$, defined as the reflected field amplitude E_r to the incident field amplitude E_i ratio at the air/graphene (or BN/air) interface.^{15,46,47} In this work, we do not consider the effect of the substrate on graphene, which can affect the plasmon polariton dispersion relationship³⁴ and not change

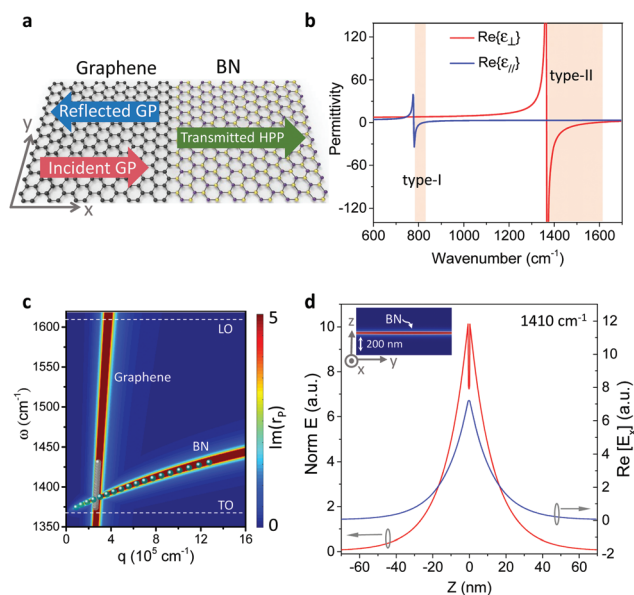


Fig. 1 (a) Schematic of the in-plane graphene/BN heterostructure. The incident GP can propagate forward until it encounters the graphene/BN interface, and then can transmit or reflect. (b) Permittivity of the BN. (c) Calculated dispersion of the GP in freestanding graphene and the HPP in freestanding BN, respectively. The Fermi energy of graphene is $E_F = 0.4$ eV. The thickness of the BN is 1 nm. Dispersion is visualized using a false-colour map of the imaginary part of the reflection coefficient r_p . The two white dashed lines exhibit the longitudinal optic (LO) and transverse optic (TO) phonons of BN. The simulation data can be illustrated as the grey and green dots. (d) The mode profile of the BN phonon polaritons with the total electric field (Norm E) and the electric field ($\text{Re}[E_x]$) along the x direction. The inset shows the spatial distribution of Norm E .

the coupling law in the graphene/BN heterostructure. For a freestanding GP, its $r_p(q, \omega)$ is as follows:⁴⁶

$$r_p(q, \omega) = \frac{4\pi k_0^2 \sigma / \omega}{2\epsilon_0 k_0 + 4\pi k_0^2 \sigma / \omega} \quad (1)$$

where ϵ_0 is the dielectric constant of air, k_0 represents the momentum of the photon in the air layer, and $\sigma = \sigma(q, \omega)$ is the in-plane optical conductivity of graphene that was obtained from the random phase approximation method.⁴⁶ The specific dielectric function of graphene^{29,48,49} is shown in Fig. S1 of the ESI.†

The BN HPP mainly depends on its hyperbolic property. The permittivity tensor of BN is diagonal, with $\epsilon_{xx} = \epsilon_{yy} = \epsilon_{\perp}$ and $\epsilon_{zz} = \epsilon_{\parallel}$ being the components perpendicular and parallel to the anisotropy axis, respectively.^{32,50,51} There are two Reststrahlen (RS) bands in BN, where the lower frequency RS band corresponds to type-I hyperbolicity ($\epsilon_{\parallel} < 0$, $\epsilon_{\perp} > 0$), and the upper RS band shows type-II hyperbolicity ($\epsilon_{\perp} < 0$, $\epsilon_{\parallel} > 0$). The RS bands are the spectral intervals between the LO and TO phonon frequencies.^{33,51} The BN permittivity (Fig. 1b) can be described using the equation:⁵¹

$$\epsilon_m = \epsilon_{\infty, m} + \epsilon_{\infty, m} \times \frac{(\omega_{LO, m})^2 - (\omega_{TO, m})^2}{(\omega_{TO, m})^2 - \omega^2 - i\omega\Gamma_m} \quad (2)$$

where $m = \perp$ and \parallel . The out-of-plane A_{2u} phonon modes of BN are $\omega_{TO} = 780 \text{ cm}^{-1}$ and $\omega_{LO} = 830 \text{ cm}^{-1}$ and the in-plane E_{1u} phonon modes are $\omega_{TO} = 1370 \text{ cm}^{-1}$ and $\omega_{LO} = 1610 \text{ cm}^{-1}$. The other parameters are $\epsilon_{\infty, \perp} = 4.87$, $\epsilon_{\infty, \parallel} = 2.95$, $\Gamma_{\perp} = 5 \text{ cm}^{-1}$ and $\Gamma_{\parallel} = 4 \text{ cm}^{-1}$.

The $r_p(q, \omega)$ of freestanding BN could be calculated as follows:¹⁵

$$r_p(q, \omega) = \frac{(1 - e^{i2k_c^z d})(\epsilon_{\perp} k_0 - \epsilon_0 k_c^z)/(\epsilon_{\perp} k_0 + \epsilon_0 k_c^z)}{1 - e^{i2k_c^z d}[(\epsilon_{\perp} k_0 - \epsilon_0 k_c^z)/(\epsilon_{\perp} k_0 + \epsilon_0 k_c^z)]^2} \quad (3)$$

where k_c^z represents the z-axis momentum of the photon in the BN layer, which is given by $k_c^z = \sqrt{\epsilon_{\perp}(\omega/c)^2 - (\epsilon_{\perp}/\epsilon_{\parallel})q^2}$, and d is the thickness of BN. In our model, d is 1 nm and the HPP response of the freestanding BN occurs in the upper RS band.

The dispersion curves of the GP and HPP are displayed by plotting the false colour map of the imaginary parts of their r_p in Fig. 1c. We also calculate their dispersion by the FEM and plot the results in Fig. 1c. The obtained grey and green dots, corresponding to GP and HPP, respectively, are consistent with the curves derived from the $r_p(q, \omega)$ theory. As can be seen, only the fundamental modes of the GP and HPP appear in the momentum space displayed in the range from 0 to $16 \times 10^5 \text{ cm}^{-1}$. And the two polariton modes can reach momentum matching at around 1385 cm^{-1} . The momentum of the BN HPP is larger than that of the GP over most of the frequency ranges. Thus the wavelength compression is more obvious in the BN HPP than that in the GP.

The BN HPP mode can be interpreted further by calculating its field profiles using the FEM. We plot the variation of the total electric field (Norm E) and the electric field x -direction

component (E_x) on the z -axis (Fig. 1d). According to the mode analysis results, Norm E is confined near the BN surface and decreases quickly moving outwards, which is a feature of surface phonon polaritons.^{52,53} The profile of the electric field x -direction component (E_x) can directly reflect the TM_0 mode because there is no node ($\text{Re}(E_x) = 0$) in the electric field distribution E_x within the BN film.⁵¹ As for the graphene plasmon, the TM mode has been widely investigated and its electromagnetic field is an evanescent wave.^{54,55}

We study the transmission of the GP and BN HPP through the graphene/BN interface by full-wave electromagnetic simulation. In the process of polariton propagation, we use a 2D model to simplify the calculation, where the computation domain is $2 \mu\text{m}$ in the propagation direction and $10 \mu\text{m}$ in the vertical propagation direction. In order to perform the boundary mode analysis of the incident port and the exit port, the ports are set to numerical ports. The whole area is surrounded by absorbing boundaries. The mesh size of the graphene/BN heterostructure is 0.1 nm and the mesh size gradually increases outside the heterostructure layer, at which the calculations reach proper convergence. A typical frequency range from 1360 to 1430 cm^{-1} covering both the GP and HPP within the upper RS band (1370 – 1610 cm^{-1}) of BN is considered. In this calculation, the absorption of the GP and BN HPP is neglected since it does not affect the resulting transmission spectra.⁵⁶ First, we calculate the transmission spectrum of the GP into the BN, shown as red diamonds in Fig. 2a. The transmittance is nearly zero at the frequency outside the RS band ($<1370 \text{ cm}^{-1}$) because there are no BN HPPs outside the RS band. In this area, for graphene, the heterostructure interface

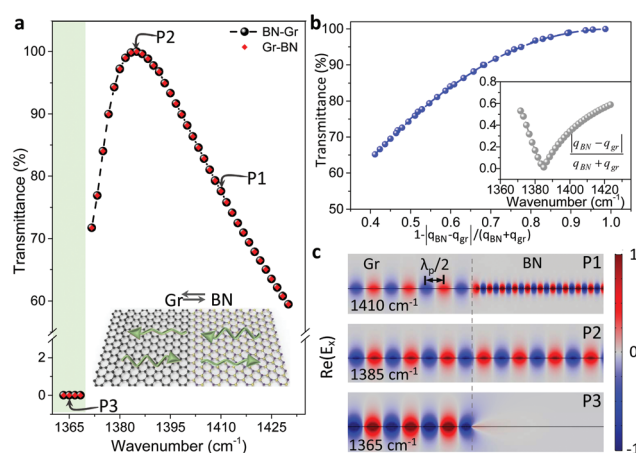


Fig. 2 (a) Transmission spectra of the GP and HPP at the graphene/BN interface. The black dashed line indicates that the BN HPP propagates into the graphene film to form GP. The red diamonds represent the opposite process of the black dashed line. These above processes are shown in the inset. (b) The transmission of the GP and HPP at the interface is closely related to the momentum matching. Inset: the momentum differences between a GP (q_{GP}) and HPP (q_{BN}) at different wavenumbers. (c) Snapshot of $\text{Re}(E_x)$ for a GP propagating into the BN. The distance between the maximum (red fringe) and minimum (blue fringe) of the electric field is half the GP wavelength, $\lambda_p/2$.

is similar to a natural edge, where the transmittance of the GP is nearly zero and the total reflection occurs.⁵⁷ The transmittance increases as the frequency increases until it reaches a maximum and then gradually decreases in the upper RS band range. The maximum transmittance is nearly 100% at a frequency of around 1385 cm^{-1} , where the GP and HPP reach the momentum matching. We also calculate the transmission of the BN HPP into the graphene plane to verify this. The calculated result (black dotted line) is completely coincident with the transmission spectrum of the GP to the HPP (red diamonds). Thus, the transmission of the GP and BN HPP does not depend on the direction of propagation of the polariton wave but is strongly related to the momentum matching.

The differences between GP and HPP momentums at different frequencies are calculated, as shown in the inset of Fig. 2b. When the frequency is around 1385 cm^{-1} , the momentum difference $|q_{\text{BN}} - q_{\text{Gr}}|/(q_{\text{BN}} + q_{\text{Gr}})$ is around zero and the two kinds of TM modes reach momentum matching. Under these conditions, the two electromagnetic modes are close to each other and the dielectric boundary almost has no effects; therefore almost 100% transmission is realized. When away from this point, the difference between the momentums of the two TM modes increases and the effects of the dielectric boundary become more severe, corresponding to decreased transmission. We plot the transmittance of the GP and HPP as a function of $1 - (|q_{\text{BN}} - q_{\text{Gr}}|/(q_{\text{BN}} + q_{\text{Gr}}))$ in Fig. 2b. As shown, the transmittance monotonically increases as the momentum matching increases.

For a deeper physical insight, we examine the spatial electromagnetic distribution of the propagating GP and HPP modes at the interface. The absorption of the GP and HPP, which does not affect transmission at the interface, is also neglected. Take the transmission of the GP into BN as an example. Fig. 2c illustrates the spatial distribution of the real part of the electrical field in the x direction E_x ($\text{Re}(E_x)$) at three typical frequencies, *i.e.*, 1410 cm^{-1} (P1), 1385 cm^{-1} (P2) and 1365 cm^{-1} (P3). They are corresponding to large transmission (P1), total transmission (P2) and total reflection (P3), respectively, which can be revealed by the electromagnetic distribution of the transmitted HPP. At P1, the wavelength of the GP is 224 nm, and when it passes through the interface and turns into a BN HPP, its wavelength is confined into 81 nm. This corresponds to a wavevector increase of $4.95 \times 10^5\text{ cm}^{-1}$ and only 77.6% of the electromagnetic energy being transferred into the BN HPP. At P2, the wavelengths of the GP and BN are exactly the same, which means perfect wavevector matching and indeed nearly 100% electromagnetic energy transmission. At P3, no electromagnetic energy can be transmitted into the BN because no HPP can be supported at this frequency.

The polariton transmission in this in-plane heterostructure can also be tuned because of the tunability of the GPs. Based on the above analysis, one of the most effective ways is changing the difference between the GP and BN HPP momentums. The GP originates from the density of electron gas and can be actively tuned by applying an electric bias. The BN polariton mode, which is from oscillations of lattice atoms in the polar

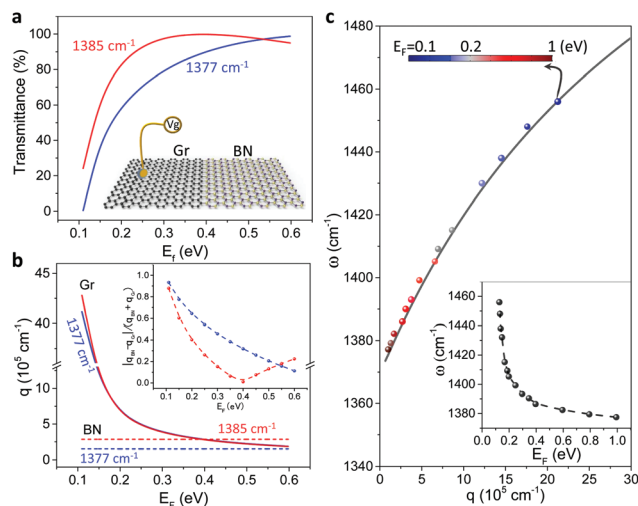


Fig. 3 (a) Transmission spectra at the selected frequencies (1385 and 1377 cm^{-1}) with the graphene Fermi energy varied from 0.1 to 0.6 eV . (b) The momentum of the GP and BN HPP at 1385 (red curve) and 1377 cm^{-1} (blue curve) with different Fermi energies. Inset: Difference in GP and BN HPP momentums at different graphene Fermi energies. (c) The grey line represents the dispersion of the BN HPP, which is calculated by the r_p theory. The dots show the cross points of the dispersion curves of the BN HPP and GP at different Fermi energies. Inset: the specific Fermi energies corresponding to different wavenumbers at 100% transmission.

crystal, is difficult to be changed.⁴⁰ Thus, we can tune the GP momentum to tune the transmission behavior in the in-plane heterostructure as shown in Fig. 2 by changing the Fermi energy (E_F) of graphene. The calculated transmission spectra for different graphene E_F values are shown in Fig. 3a. Two typical frequencies (1385 and 1377 cm^{-1}) of polaritons are selected, and the results at other frequencies are similar. It can be seen that transmittance can almost increase from almost 0% to 100% as E_F increases, reaching a maximum and then slowly decreases. At different frequencies, the transmittance maximum occurs at different graphene Fermi energies.

The electrical tunability of transmission is directly determined by the momentum matching of different polaritons. The GP and BN HPP momentums corresponding to Fig. 3a are illustrated in Fig. 3b. The BN HPP momentum remains constant, while the GP momentum gradually decreases as the Fermi energy increases, following the equation $q \propto \omega_{\text{pl}}^2/E_F$.^{29,58} The GP momentum is larger than the BN HPP momentum at lower E_F . Thus the GP momentum is gradually close to the BN HPP momentum and the momentum difference decreases as the Fermi energy increases (Fig. 3b, inset). When the momentum curves of the GP and BN HPP intercross, the transmittance is the largest ($\sim 100\%$), as the condition for the frequency of 1385 cm^{-1} with $E_F = 0.4\text{ eV}$. Because of the large tunable momentum difference, we can realize a wide range modulation of transmittance from 0% to 100%. This transmittance modulation can be achieved over a large spectral range. By changing the graphene Fermi energy, we can control the graphene plasmon dispersion as shown in Fig. S5 of the ESI,[†] which will

change the intersection of graphene plasmon dispersion and BN phonon polariton dispersion. In Fig. 3c, we calculate the different momentum cross points at different graphene Fermi energies. These cross points show momentum matching, indicating that the transmittance will be around 100%. These cross points can occur in the frequency range of the BN HPP (1370–1460 cm^{-1}), while the graphene Fermi energy varies from 0.1 to 1 eV. Therefore, by changing the graphene Fermi energy from the outside, we can achieve dynamic tunability of the transmission of polaritons in a wide frequency range in the in-plane heterostructure.

The transmission of different polariton waves can be characterized using near-field microscopy. In particular, s-SNOM is the most effective experimental instrument to visualize the GP and BN HPP in real space. In a typical s-SNOM experiment, an infrared laser beam illuminates the AFM tip of the s-SNOM. The tip can strongly confine the laser beam at the tip apex, providing the momentum needed to launch GP or BN HPP.^{56,59} When propagating polaritons reflect at a boundary, characteristic interference patterns are formed and can be scattered into the detector by the s-SNOM tip, and thus be measured in the near-field images. We numerically simulate a potential s-SNOM experiment to obtain the near-field images and calculate the reflection (or transmission) of the GP and HPP at the interface.

As previously reported, the vertical component of the electric field (E_z) below the dipole source can serve as a good qualitative approximation for the s-SNOM near-field signal.^{59,60} We simulate the near-field interference patterns of the GP and HPP at the graphene/BN boundary and a natural graphene edge (graphene/air), as shown in Fig. 4b. The latter is used as a control experiment.⁵⁷ In this simulation, $|E_z/E_{z0}|$ is adapted, where E_{z0} represents the z-component of the electric field without graphene. And the absorption of graphene and BN has been taken into account by retaining the imaginary part of the graphene and BN permittivities.⁵⁶ From all the near-field interference patterns in Fig. 4b, we can observe fringes parallel to the boundaries indicating the interference of the launched GP (or BN HPP) and the reflected GP (or BN HPP) by the boundary, but the signal strength changes as the frequency varies.

To further analyze the near-field interference patterns, the line profiles of the fringes are extracted along the direction perpendicular to the boundaries (Fig. 4c). The distances between the adjacent peaks (or dips) far from the boundary are half of the wavelength, $\lambda_p/2$. Due to the finite propagation length of the GP and BN HPP, the amplitude of the fringes decays along the graphene or BN in both directions across the boundary. However, transmission (or reflection) at the interface is almost transient and the energy loss of polaritons can be ignored. The reflectivity (or transmittance) can be extracted from the near-field profiles described below. The reflection of the GP at a natural boundary can be considered as nearly 100%.⁵⁷ We calculate the difference between peak 1 (orange dot in Fig. 4c) and dip 1 (grey dot in Fig. 4c) in $|E_z/E_{z0}|$ profiles as the near-field signal of the graphene natural edge bright

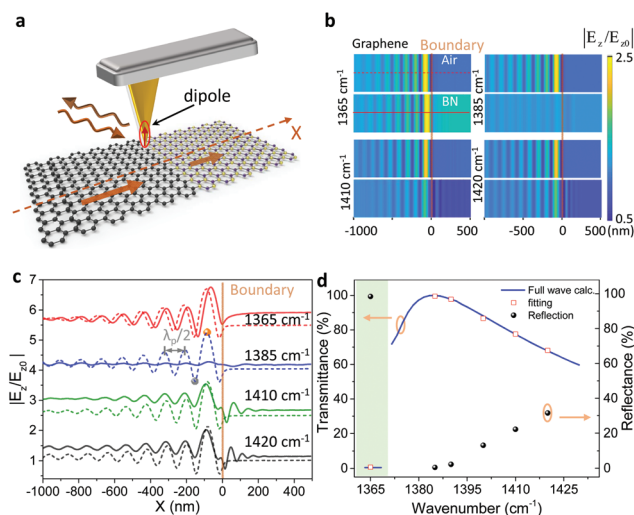


Fig. 4 (a) Schematics of the simulation in s-SNOM experiments. The atomic force microscope (AFM) tip is approximated using a simple electric dipole point-source. The dipole is 100 nm above graphene. (b) The simulated near-field image $|E_z(x,y)|$ of graphene/air (top part) and graphene/BN (bottom part) at different wavenumbers. (c) Line profile, $|E_z(x)|$, normalized to the value of the field ($|E_{z0}(x)|$) without 2D materials (air area). The solid (dashed) line is extracted from the graphene/BN (graphene/air) at different wavenumbers in 3b. The orange line shows the graphene/BN and graphene/air boundaries. (d) Transmission spectra are calculated by the full-wave simulation (solid line) and extracted from the near-field line profiles (squares). The graphene charge carrier relaxation time $\tau = 0.08$ ps.

line ($\sqrt{S_{\text{edge}}}$). Finally, the graphene plasmon reflection can be estimated using the equation $r = (S_{\text{gt-BN}} - |E_{z0}/E_{z0}|^2)/(S_{\text{edge}} - |E_{z0}/E_{z0}|^2)$, where $S_{\text{gt-BN}}$ is the near-field energy signal for the graphene/BN interface bright line.^{57,61} Thus the reflections with different frequencies are shown in Fig. 4d (as solid black circles). Then the transmittance is calculated, which is in accordance with the results of the full wave calculations shown in Fig. 2a.

Conclusions

In conclusion, we have proposed a full-wave electromagnetic numerical model to solve polariton transmission at the interface of the in-plane graphene and BN heterostructures, which provides a key foundation for designing in-plane integrated optics. Transmittance of different polaritons is inversely proportional to their momentum difference. Changing the degree to which the momentums matched by altering the graphene Fermi energy (between 0.1 and 1 eV) would allow polariton transmission to be tuned from 0% to 100% in the upper RS band of BN. Based on high-efficiency modulation of transmittance, we further demonstrate the microscopic process of electromagnetic transmission through simulating near-field interference patterns of polaritons, which is in good agreement with the numerical model. The near field interference patterns would be measured by s-SNOM, which provides a potential

experimental method to investigate the coupling of different polaritons in the in-plane heterostructure. This study provides a new theoretical basis for investigating the in-plane coupling of different polaritons in 2D vdW materials, and offers promise for designing ultra-compact functional optical devices such as modulators, low loss waveguides, and filters.

Conflicts of interest

There are no conflicts to declare.

Acknowledgements

This work was supported by the National Basic Key Research Program of China (Grant No. 2015CB932402), the National Key Research and Development Program of China (Grant No. 2016YFA0201600), the National Natural Science Foundation of China (Grant No. 11504063, 11674073, 11704085, and 11427808), the Bureau of International Cooperation, the key program of the Bureau of Frontier Sciences and Education, Chinese Academy of Sciences (QYZDB-SSW-SLH021), the Key Project of Chinese Academy of Sciences (ZDBS-SSW-JSC002) and Strategic Priority Research Program of Chinese Academy of Sciences (Grant No. XDB30000000).

References

- B. Shen, R. Polson and R. Menon, *Nat. Commun.*, 2016, **7**, 13126.
- Y. Fang and M. Sun, *Light: Sci. Appl.*, 2015, **4**, e294.
- J. Chen, M. Badioli, P. Alonso-Gonzalez, S. Thongrattanasiri, F. Huth, J. Osmond, M. Spasenovic, A. Centeno, A. Pesquera, P. Godignon, A. Z. Elorza, N. Camara, F. J. Garcia de Abajo, R. Hillenbrand and F. H. Koppens, *Nature*, 2012, **487**, 77–81.
- Z. Fei, A. S. Rodin, G. O. Andreev, W. Bao, A. S. McLeod, M. Wagner, L. M. Zhang, Z. Zhao, M. Thiemens, G. Dominguez, M. M. Fogler, A. H. Castro Neto, C. N. Lau, F. Keilmann and D. N. Basov, *Nature*, 2012, **487**, 82–85.
- P. Li, I. Dolado, F. J. Alfaro-Mozaz, F. Casanova, L. E. Hueso, S. Liu, J. H. Edgar, A. Y. Nikitin, S. Vézé and R. Hillenbrand, *Science*, 2018, **359**, 892–896.
- F. Xia, H. Wang, D. Xiao, M. Dubey and A. Ramasubramaniam, *Nat. Photonics*, 2014, **8**, 899–907.
- D. N. Basov, M. M. Fogler and F. J. Garcia de Abajo, *Science*, 2016, **354**, aag1992.
- T. Low, A. Chaves, J. D. Caldwell, A. Kumar, N. X. Fang, P. Avouris, T. F. Heinz, F. Guinea, L. Martin-Moreno and F. Koppens, *Nat. Mater.*, 2017, **16**, 182–194.
- K. S. Novoselov, A. Mishchenko, A. Carvalho and A. H. Castro Neto, *Science*, 2016, **353**, aac9439.
- G. X. Ni, L. Wang, M. D. Goldflam, M. Wagner, Z. Fei, A. S. McLeod, M. K. Liu, F. Keilmann, B. Özyilmaz, A. H. Castro Neto, J. Hone, M. M. Fogler and D. N. Basov, *Nat. Photonics*, 2016, **10**, 244–247.
- G. X. Ni, A. S. McLeod, Z. Sun, L. Wang, L. Xiong, K. W. Post, S. S. Sunku, B. Y. Jiang, J. Hone, C. R. Dean, M. M. Fogler and D. N. Basov, *Nature*, 2018, **557**, 530–533.
- M. A. Huber, F. Mooshammer, M. Plankl, L. Viti, F. Sandner, L. Z. Kastner, T. Frank, J. Fabian, M. S. Vitiello, T. L. Cocker and R. Huber, *Nat. Nanotechnol.*, 2017, **12**, 207–211.
- Z. Liu and K. Aydin, *Nano Lett.*, 2016, **16**, 3457–3462.
- F. Hu, Y. Luan, M. E. Scott, J. Yan, D. G. Mandrus, X. Xu and Z. Fei, *Nat. Photonics*, 2017, **11**, 356–360.
- S. Dai, Z. Fei, Q. Ma, A. S. Rodin, M. Wagner, A. S. McLeod, M. K. Liu, W. Gannett, W. Regan, K. Watanabe, T. Taniguchi, M. Thiemens, G. Dominguez, A. H. C. Neto, A. Zettl, F. Keilmann, P. Jarillo-Herrero, M. M. Fogler and D. N. Basov, *Science*, 2014, **343**, 1125–1129.
- A. A. Goyvadinov, A. Konecna, A. Chuvilin, S. Velez, I. Dolado, A. Y. Nikitin, S. Lopatin, F. Casanova, L. E. Hueso, J. Aizpurua and R. Hillenbrand, *Nat. Commun.*, 2017, **8**, 95.
- H. Yan, X. Li, B. Chandra, G. Tulevski, Y. Wu, M. Freitag, W. Zhu, P. Avouris and F. Xia, *Nat. Nanotechnol.*, 2012, **7**, 330–334.
- S. Kim, M. S. Jang, V. W. Brar, K. W. Mauser, L. Kim and H. A. Atwater, *Nano Lett.*, 2018, **18**, 971–979.
- L. Ju, B. Geng, J. Horng, C. Girit, M. Martin, Z. Hao, H. A. Bechtel, X. Liang, A. Zettl, Y. R. Shen and F. Wang, *Nat. Nanotechnol.*, 2011, **6**, 630–634.
- H. Hu, F. Zhai, D. Hu, Z. Li, B. Bai, X. Yang and Q. Dai, *Nanoscale*, 2015, **7**, 19493–19500.
- T. Low, R. Roldan, H. Wang, F. Xia, P. Avouris, L. M. Moreno and F. Guinea, *Phys. Rev. Lett.*, 2014, **113**, 106802.
- I.-H. Lee, L. Martin-Moreno, D. A. Mohr, K. Khaliji, T. Low and S.-H. Oh, *ACS Photonics*, 2018, **5**, 2208–2216.
- A. J. Giles, S. Dai, I. Vurgaftman, T. Hoffman, S. Liu, L. Lindsay, C. T. Ellis, N. Assefa, I. Chatzakis, T. L. Reinecke, J. G. Tischler, M. M. Fogler, J. H. Edgar, D. N. Basov and J. D. Caldwell, *Nat. Mater.*, 2018, **17**, 134–139.
- S. Dai, Q. Ma, M. K. Liu, T. Andersen, Z. Fei, M. D. Goldflam, M. Wagner, K. Watanabe, T. Taniguchi, M. Thiemens, F. Keilmann, G. C. Janssen, S. E. Zhu, P. Jarillo-Herrero, M. M. Fogler and D. N. Basov, *Nat. Nanotechnol.*, 2015, **10**, 682–686.
- M. Tamagnone, A. Ambrosio, K. Chaudhary, L. A. Jauregui, P. Kim, W. L. Wilson and F. Capasso, *Sci. Adv.*, 2018, **4**, eaat7189.
- X. Guo, H. Hu, B. Liao, X. Zhu, X. Yang and Q. Dai, *Nanotechnology*, 2018, **29**, 184004.
- D. Rodrigo, O. Limaj, D. Janner, D. Etezadi, F. J. Garcia de Abajo, V. Pruneri and H. Altug, *Science*, 2015, **349**, 165–168.
- H. Hu, X. Yang, F. Zhai, D. Hu, R. Liu, K. Liu, Z. Sun and Q. Dai, *Nat. Commun.*, 2016, **7**, 12334.
- X. Guo, H. Hu, X. Zhu, X. Yang and Q. Dai, *Nanoscale*, 2017, **9**, 14998–15004.

- 30 X. Yang, Z. Sun, T. Low, H. Hu, X. Guo, F. J. Garcia de Abajo, P. Avouris and Q. Dai, *Adv. Mater.*, 2018, **30**, e1704896.
- 31 M. Autore, P. Li, I. Dolado, F. J. Alfaro-Mozaz, R. Esteban, A. Atxabal, F. Casanova, L. E. Hueso, P. Alonso-González, J. Aizpurua, A. Y. Nikitin, S. Vélez and R. Hillenbrand, *Light: Sci. Appl.*, 2018, **7**, 17172.
- 32 S. Dai, Q. Ma, T. Andersen, A. S. McLeod, Z. Fei, M. K. Liu, M. Wagner, K. Watanabe, T. Taniguchi, M. Thiemens, F. Keilmann, P. Jarillo-Herrero, M. M. Fogler and D. N. Basov, *Nat. Commun.*, 2015, **6**, 6963.
- 33 P. Li, M. Lewin, A. V. Kretinin, J. D. Caldwell, K. S. Novoselov, T. Taniguchi, K. Watanabe, F. Gaussmann and T. Taubner, *Nat. Commun.*, 2015, **6**, 7507.
- 34 X. Yang, F. Zhai, H. Hu, D. Hu, R. Liu, S. Zhang, M. Sun, Z. Sun, J. Chen and Q. Dai, *Adv. Mater.*, 2016, **28**, 2931–2938.
- 35 A. Woessner, M. B. Lundeberg, Y. Gao, A. Principi, P. Alonso-Gonzalez, M. Carrega, K. Watanabe, T. Taniguchi, G. Vignale, M. Polini, J. Hone, R. Hillenbrand and F. H. Koppens, *Nat. Mater.*, 2015, **14**, 421–425.
- 36 X. Yang, X. T. Kong, B. Bai, Z. Li, H. Hu, X. Qiu and Q. Dai, *Small*, 2015, **11**, 591–596.
- 37 H. Yan, T. Low, W. Zhu, Y. Wu, M. Freitag, X. Li, F. Guinea, P. Avouris and F. Xia, *Nat. Photonics*, 2013, **7**, 394.
- 38 I. Soto Lamata, P. Alonso-González, R. Hillenbrand and A. Y. Nikitin, *ACS Photonics*, 2015, **2**, 280–286.
- 39 A. Y. Nikitin, P. Alonso-Gonzalez and R. Hillenbrand, *Nano Lett.*, 2014, **14**, 2896–2901.
- 40 M. Maier, A. Nemilentsau, T. Low and M. Luskina, *ACS Photonics*, 2017, **5**, 544–551.
- 41 L. Liu, J. Park, D. A. Siegel, K. F. McCarty, K. W. Clark, W. Deng, L. Basile, J. C. Idrobo, A.-P. Li and G. Gu, *Science*, 2014, **343**, 163–167.
- 42 T. Gao, X. Song, H. Du, Y. Nie, Y. Chen, Q. Ji, J. Sun, Y. Yang, Y. Zhang and Z. Liu, *Nat. Commun.*, 2015, **6**, 6835.
- 43 M. P. Levendorf, C. J. Kim, L. Brown, P. Y. Huang, R. W. Havener, D. A. Muller and J. Park, *Nature*, 2012, **488**, 627–632.
- 44 Z. Liu, L. Ma, G. Shi, W. Zhou, Y. Gong, S. Lei, X. Yang, J. Zhang, J. Yu, K. P. Hackenberg, A. Babakhani, J. C. Idrobo, R. Vajtai, J. Lou and P. M. Ajayan, *Nat. Nanotechnol.*, 2013, **8**, 119–124.
- 45 D. Hu, X. Yang, C. Li, R. Liu, Z. Yao, H. Hu, S. N. G. Corder, J. Chen, Z. Sun, M. Liu and Q. Dai, *Nat. Commun.*, 2017, **8**, 1471.
- 46 Z. Fei, G. O. Andreev, W. Bao, L. M. Zhang, S. M. Alexander, C. Wang, M. K. Stewart, Z. Zhao, G. Dominguez, M. Thiemens, M. M. Fogler, M. J. Tauber, A. H. Castro-Neto, C. N. Lau, F. Keilmann and D. N. Basov, *Nano Lett.*, 2011, **11**, 4701–4705.
- 47 Z. Fei, M. D. Goldflam, J. S. Wu, S. Dai, M. Wagner, A. S. McLeod, M. K. Liu, K. W. Post, S. Zhu, G. C. Janssen, M. M. Fogler and D. N. Basov, *Nano Lett.*, 2015, **15**, 8271–8276.
- 48 S.-X. Xia, X. Zhai, L.-L. Wang and S.-C. Wen, *Photonics Res.*, 2018, **6**, 692–702.
- 49 S. X. Xia, X. Zhai, L. L. Wang, B. Sun, J. Q. Liu and S. C. Wen, *Opt. Express*, 2016, **24**, 17886–17899.
- 50 J. Duan, R. Chen, J. Li, K. Jin, Z. Sun and J. Chen, *Adv. Mater.*, 2017, **29**, 1702494.
- 51 A. Kumar, T. Low, K. H. Fung, P. Avouris and N. X. Fang, *Nano Lett.*, 2015, **15**, 3172–3180.
- 52 A. Y. Nikitin, E. Yoxall, M. Schnell, S. Vélez, I. Dolado, P. Alonso-Gonzalez, F. Casanova, L. E. Hueso and R. Hillenbrand, *ACS Photonics*, 2016, **3**, 924–929.
- 53 P. Li, I. Dolado, F. J. Alfaro-Mozaz, A. Y. Nikitin, F. Casanova, L. E. Hueso, S. Vélez and R. Hillenbrand, *Nano Lett.*, 2016, **17**, 228–235.
- 54 S. A. Mikhailov and K. Ziegler, *Phys. Rev. Lett.*, 2007, **99**, 016803.
- 55 C. H. Gan, H. S. Chu and E. P. Li, *Phys. Rev. B: Condens. Matter Mater. Phys.*, 2012, **85**, 124531.
- 56 T. M. Slipchenko, M. L. Nesterov, R. Hillenbrand, A. Y. Nikitin and L. Martín-Moreno, *ACS Photonics*, 2017, **4**, 3081–3088.
- 57 L. Jiang, Z. Shi, B. Zeng, S. Wang, J. H. Kang, T. Joshi, C. Jin, L. Ju, J. Kim, T. Lyu, Y. R. Shen, M. Crommie, H. J. Gao and F. Wang, *Nat. Mater.*, 2016, **15**, 840–844.
- 58 S. H. Abedinpour, G. Vignale, A. Principi, M. Polini, W.-K. Tse and A. H. MacDonald, *Phys. Rev. B: Condens. Matter Mater. Phys.*, 2011, **84**, 045429.
- 59 A. Y. Nikitin, P. Alonso-González, S. Vélez, S. Mastel, A. Centeno, A. Pesquera, A. Zurutuza, F. Casanova, L. E. Hueso, F. H. L. Koppens and R. Hillenbrand, *Nat. Photonics*, 2016, **10**, 239–243.
- 60 F. Hu, Y. Luan, Z. Fei, I. Z. Palubski, M. D. Goldflam, S. Dai, J. S. Wu, K. W. Post, G. Janssen, M. M. Fogler and D. N. Basov, *Nano Lett.*, 2017, **17**, 5423–5428.
- 61 S. Dai, M. Tymchenko, Y. Yang, Q. Ma, M. Pita-Vidal, K. Watanabe, T. Taniguchi, P. Jarillo-Herrero, M. M. Fogler, A. Alu and D. N. Basov, *Adv. Mater.*, 2018, **30**, e1706358.